

MOF-Derived Porous Carbon for Zinc-ion Hybrid Capacitors with Ultra-High Energy Density and Long Cycling Life

Junjie Zhang,^[a] Xiang Wu,^{*[a]} and Shaohua Luo^{*[b]}

Zinc-ion hybrid capacitors (ZHC) have been considered as emerging sustainable electrochemical energy storage devices. They integrate the benefits of high-energy density of aqueous zinc ion battery (ZIB) with high-power density of supercapacitor (SC). Metal-organic frameworks (MOFs) have been widely used to design electrode materials for portable devices, especially in some energy storage fields because of their large specific

surface area and adjustable pore structures. In this work, we prepare porous $\text{Mn}_3\text{O}_4/\text{C}$ nanosheets with Mn-BDC as a precursor. The assembled device delivers a specific capacitance of 155.3 mAh g^{-1} at a current of 3 A g^{-1} and keeps a retention rate of 97.7% after 10,000 cycles. Moreover, it provides an energy density of 464.5 Wh kg^{-1} at a power density of 100 W kg^{-1} .

1. Introduction

In the past few years, rapid economic development has led to a significant increase in global energy demand.^[1] While the excessive consumption of fossil fuels has aggravated serious environmental pollution and resource shortages.^[2] Therefore, it is imperative to exploit renewable and sustainable energy technologies.^[3] So far, various rechargeable energy storage devices have been developed to alleviate present energy shortage.^[4] In particular, lithium-ion batteries (LIBs) have been widely used in current battery markets due to their high energy density.^[5] Nevertheless, besides some safety issues associated with LIBs, the limited lithium resources make lithium-containing materials expensive.^[6] The development of supercapacitors has been restricted due to their low energy density despite their high-power density and long-term cycle stability.^[7] Zinc-ion hybrid capacitor (ZHC), as an emerging energy storage equipment, has been research focuses owing to its features of low-cost, high power and recyclability.^[8–10]

The electrode materials for the ZHCs include capacitor-type and battery-type ones.^[11] Capacitive materials provide enhanced cycling performance because of the adsorption/desorption of zinc ions;^[12] while battery-type materials possess high specific capacity based on the embedding/de-embedding of zinc ions.^[13,14] Unfortunately, the former presents relatively low specific capacity, while the latter shows poor cycling performance.^[15] Therefore, the key to enhance the performance of the ZHCs depends on rational design of high-performance and stable electrode materials.^[16–18] Currently, capacitive materials applied for the ZHCs are mainly based on carbon materials,

including activated carbon (AC), carbon nanotubes (CNTs), graphene, and nanoporous carbon (PC).^[19–22]

Up to now, zinc-ion hybrid capacitors still face many challenges, such as fast ion adsorption/desorption on carbon-based cathode and the slow zinc deposition/desorption on zinc anode. The different energy storage mechanisms lead to mismatch of the energy storage rate between electrodes, which limits the power output of the hybrid capacitor.^[23] In previous reports, Dong et al. prepared AC//Zn capacitors with 2 mol L^{-1} of ZnSO_4 electrolyte, which achieve a capacity of 121 mAh g^{-1} at 0.1 A g^{-1} , and maintain 91% capacity retention rate after 10,000 times cycling.^[24] Chen and co-workers designed copolymer-derived hollow carbon spheres, by which the assembled flexible devices show a capacity of 86.8 mAh g^{-1} at 0.5 A g^{-1} .^[25] Their devices could even achieve an energy density of 59.7 Wh kg^{-1} at a power density of 447.8 W kg^{-1} . The Huang group designed N, O, F co-doped porous carbon as cathode,^[26] which presents a capacity of 168.4 mAh g^{-1} and an energy density of 131.9 Wh kg^{-1} at 0.5 A g^{-1} . Although these achievements have been reached, a challenging task remains to quantitatively integrate dopants into porous carbon.

Metal-organic framework (MOF) materials are co-constructed by metal ions (or clusters) as the center ion and organic ligands through chemical bonding.^[27] The composition and structure of MOFs are designed by choosing different metal ions (usually transition metal ions, such as Zn^{2+} , Fe^{3+} , Co^{2+} , etc.) as nodes and different organic ligands.^[28] One can choose suitable precursors to adjust the composition and morphology of carbon products. In this work, we synthesize Mn-BDC materials with polyhedral morphology as precursor through a hydrothermal route. Then a high temperature pyrolysis process is used to prepare three-dimensional porous $\text{Mn}_3\text{O}_4/\text{C}$ materials. The unique structure endows the electrodes with a large specific surface area and high electrical conductivity. The assembled $\text{Mn}_3\text{O}_4/\text{C}/\text{Zn}$ device possesses a specific capacity of 155.3 mAh g^{-1} at the current density of 3 A g^{-1} and keeps the retention rate of 97.7% after 10,000 cycles.

[a] J. Zhang, X. Wu
School of Materials Science and Engineering, Shenyang University of Technology,
Shenyang 110870, P. R. China
E-mail: wuxiang05@sut.edu.cn

[b] S. Luo
Hebei Key Laboratory of Dielectric and Electrolyte Functional Material,
Northeastern University at Qinhuangdao, Qinhuangdao 066004, P. R. China
E-mail: luosh@neuq.edu.cn

Experimental Section

All the chemicals were used as purchased. Firstly, 2 mmol MnO_2 powder and 8.4 mmol terephthalic acid (H_2BDC) were put into 60 mL of deionized water. After stirring for 5 min, 2 mmol ascorbic acid ($\text{C}_6\text{H}_8\text{O}_6$) was added as a reducing agent and stirring continued until the solid was dissolved. Subsequently, the solution was transferred into a 100-mL high-pressure reactor and heated at 180 °C for 12 h. After that, the solution was washed with DL and anhydrous ethanol, respectively, and then dried in a vacuum oven at 60 °C overnight. The obtained gray powder was recorded as the precursor (Mn-BDC).

The precursors were then carbonized in a tube furnace under argon atmosphere at different temperatures (700 °C, 600 °C and 800 °C) for 3 h at an increasing rate of 5 °C min⁻¹. The final samples were etched with 1 M HCl solution to remove the excess manganese elements and dried at 60 °C for 12 h. The products obtained were noted as $\text{Mn}_3\text{O}_4/\text{C}-700$, $\text{Mn}_3\text{O}_4/\text{C}-600$ and $\text{Mn}_3\text{O}_4/\text{C}-800$, respectively.

The crystal structures of the samples were studied by X-ray powder diffractometer (XRD Shimadzu-7000, Cu $\text{K}\alpha$ radiation, $\lambda=0.1541 \text{ nm}$, 40 KV) and X-ray photoelectron spectroscopy (XPS, Thermo Scientific K α , Waltham). A nitrogen (N_2) adsorption/desorption analyzer (JW-TB 200) was used to characterize the specific surface area and pore size distribution of the materials via Brunauer-Emmett-Teller (BET) method. The morphology and elemental composition were observed by scanning electron microscope (SEM, Gemini 300-71-31).

The active material ($\text{Mn}_3\text{O}_4/\text{C}$), acetylene black and polyvinylidene fluoride (PVDF) were mixed homogeneously into N-methyl-2-pyrrolidone (NMP) with a mass ratio of 7:2:1. The above paste was pressed onto a carbon paper with a diameter of 1 cm and dried under vacuum at 60 °C for 12 h. Then, the CR2032 button batteries

were assembled using zinc foil as anode and the as-obtained sample as cathode. The electrolyte is weakly acidic 2 M $\text{ZnSO}_4+0.2 \text{ M MnSO}_4$ solution. The average loading mass of cathode is 1.5 mg cm⁻². An automated battery tester (Neware, CT-4008 T) was used to test the electrochemical performance of the batteries. Cyclic voltammetry (CV) and electrochemical impedance spectroscopy (EIS) tests were also performed on a CHI660E electrochemical workstation.

2. Result and Discussion

Firstly, we investigate the crystallinity and structure of the $\text{Mn}_3\text{O}_4/\text{C}$ materials by XRD. The major diffraction peaks are 29.9°, 35.5°, 43.0°, 56.8° and 62.3°, corresponding to the crystallographic planes (220), (311), (400), (511), and (440), respectively (Figure 1a). In addition, there are no other redundant peaks appearing, which indicate the high crystalline of the samples. It can be observed that the diffraction peak at 26.6° corresponds to the crystal plane (002) of carbon. The peak with high diffraction intensity indicates the high graphitization of the calcined composite. The surface compositions and chemical states of the samples are further investigated by X-ray photoelectron spectroscopy (XPS). The full XPS spectrum confirms the presence of Mn, O and C elements in $\text{Mn}_3\text{O}_4/\text{C}$ samples (Figure 1b). Three characteristic peaks are presented in the fitted C 1s spectrum (Figure 1c), which belong to C–C, C–O–C, and O=C=O bonds, respectively.^[29] From the Mn 2p spectrum (Figure 1d), the binding energies of Mn 2p_{1/2} and Mn 2p_{3/2} are

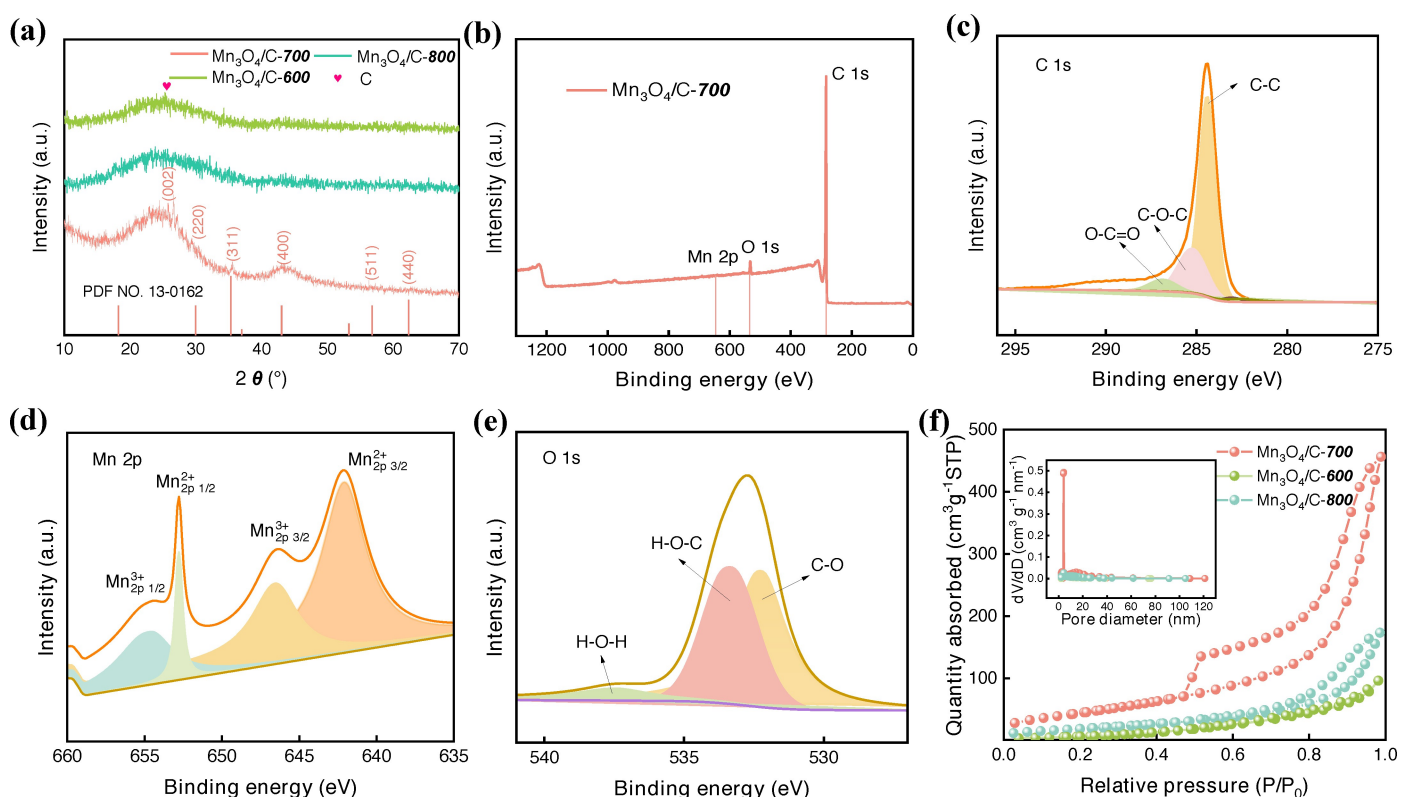


Figure 1. Structure characterizations of the samples (a) XRD patterns (b) XPS survey spectra (c–e) XPS spectra of C 1s Mn 2p and O 1s of $\text{Mn}_3\text{O}_4/\text{C}$ samples (f) N_2 adsorption-desorption isotherms of $\text{Mn}_3\text{O}_4/\text{C}$ samples.

located at 652.78 and 642.08 eV, respectively, which correspond to Mn²⁺. The peaks at 654.58 and 646.68 eV belong to Mn³⁺. Mn₃O₄ with mixed valences (Mn³⁺, Mn²⁺) can enhance the electrochemical activity of the cathode material.^[30] In Figure 1e, the O 1s spectrum fits with C—O bonds (532.28 eV), H—O—C bonds (533.38 eV) and H—O—H bonds (537.48 eV).^[31]

N₂ adsorption/desorption tests are then carried out to evaluate the specific surface area and pore size distribution (Figure 1(f)). According to BET classification, the curves are type IV isotherms and show H3-type hysteresis loops, which exhibit typical mesopore structure. In table 1, the specific surface areas of Mn₃O₄/C-700, Mn₃O₄/C-600 and Mn₃O₄/C-800 samples are 170.95 cm²g⁻¹, 47.66 cm²g⁻¹ and 72.49 cm²g⁻¹, respectively. Furthermore, the total pore content of the former (0.706 cm³g⁻¹) is larger than that of the latter two (0.179 cm³g⁻¹ and 0.268 cm³g⁻¹). The larger specific surface area provides many active sites, favorable for improving the surface pseudo-capacitance of the material. The inset presents the pore size distribution of the Mn₃O₄/C samples, demonstrating both micropores and mesopores of the structure. According

to previous report, the former can enhance the double electric layer capacitance of the material and the latter reduce the impedance of ion transport.^[32] Their simultaneous presence can enhance the electrochemical activity and active sites, which effectively adapt volume expansion during reactions.

Figure 2a shows the SEM image of the samples. It is found that the Mn-BDC precursor presents a randomly arranged multiple layers. We use Mn-BDC as a self-sacrificial template to obtain Mn₃O₄/C samples after high-temperature pyrolysis and acid washing. From Figure 2b–2d, due to the gradual decomposition of organic ligands to release gaseous molecules (e.g., CO₂ and H₂O), the regular structure of MOFs slightly collapses, leading to a decrease in porosity. On the other hand, acid washing can increase the porosity of the material by removing metal components appropriately. The metal ion nodes are converted in situ to metal oxides during high-temperature carbonization. Its rigid character allows the morphological features of the precursor to be maintained. Therefore, all the carbonized products basically keep the nanosheet morphology. However, its surface pore structure changes with the temperature of pyrolysis. The SEM images reveal many filamentous structures on the surface of Mn₃O₄/C-700 samples (Figure 2b). The SEM images of Mn₃O₄/C-600, Mn₃O₄/C-800 materials show their smooth and flat surfaces. This lack of pore morphology makes the active sites of the samples much low.

After that, we assemble many ZHC devices to explore the electrochemical properties of the synthesized materials. Figure 3a demonstrates the schematic of the electrochemical reaction mechanism of the capacitor. During the reaction,

Table 1. Specific surface areas, total pore volumes and average pore diameter of the synthesized samples.

Samples	Specific Surface Area [m ² /g]	Total Pore Volume [cm ³ /g]	Average Pore Diameter [nm]
Mn ₃ O ₄ /C-600	47.66	0.149	15.511
Mn ₃ O ₄ /C-800	72.49	0.268	14.803
Mn ₃ O ₄ /C-700	170.95	0.706	16.525

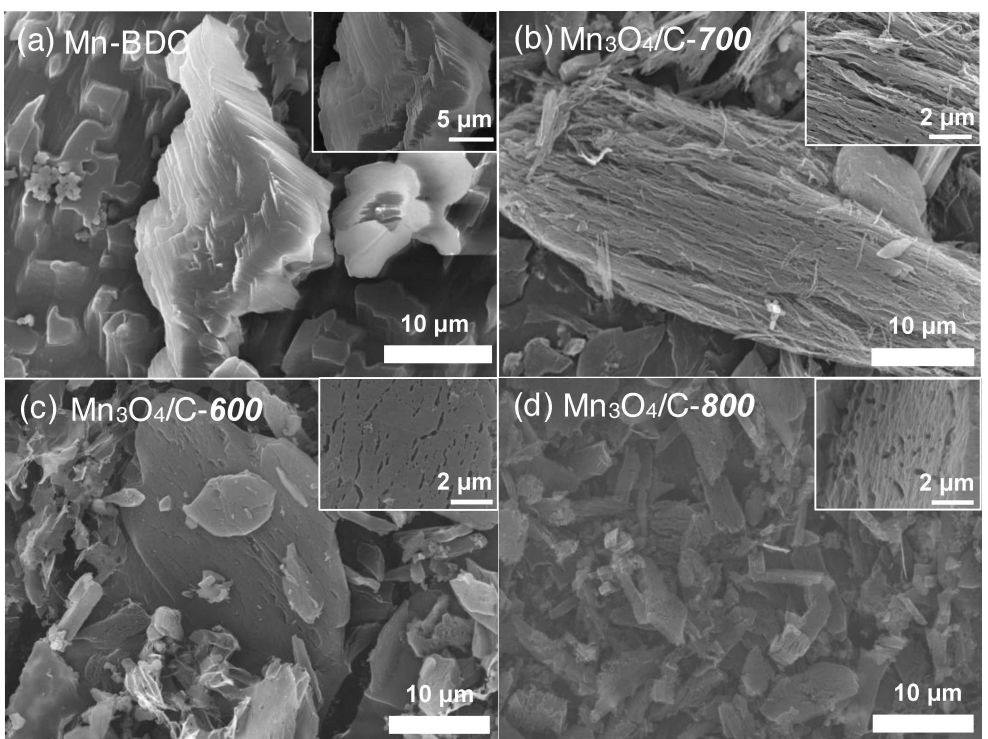


Figure 2. Morphology characterization (a) SEM images of Mn-BDC sample (b) SEM images of the Mn₃O₄/C-700 sample (c) SEM images of the Mn₃O₄/C-600 sample and (d) SEM images of the Mn₃O₄/C-800 sample.

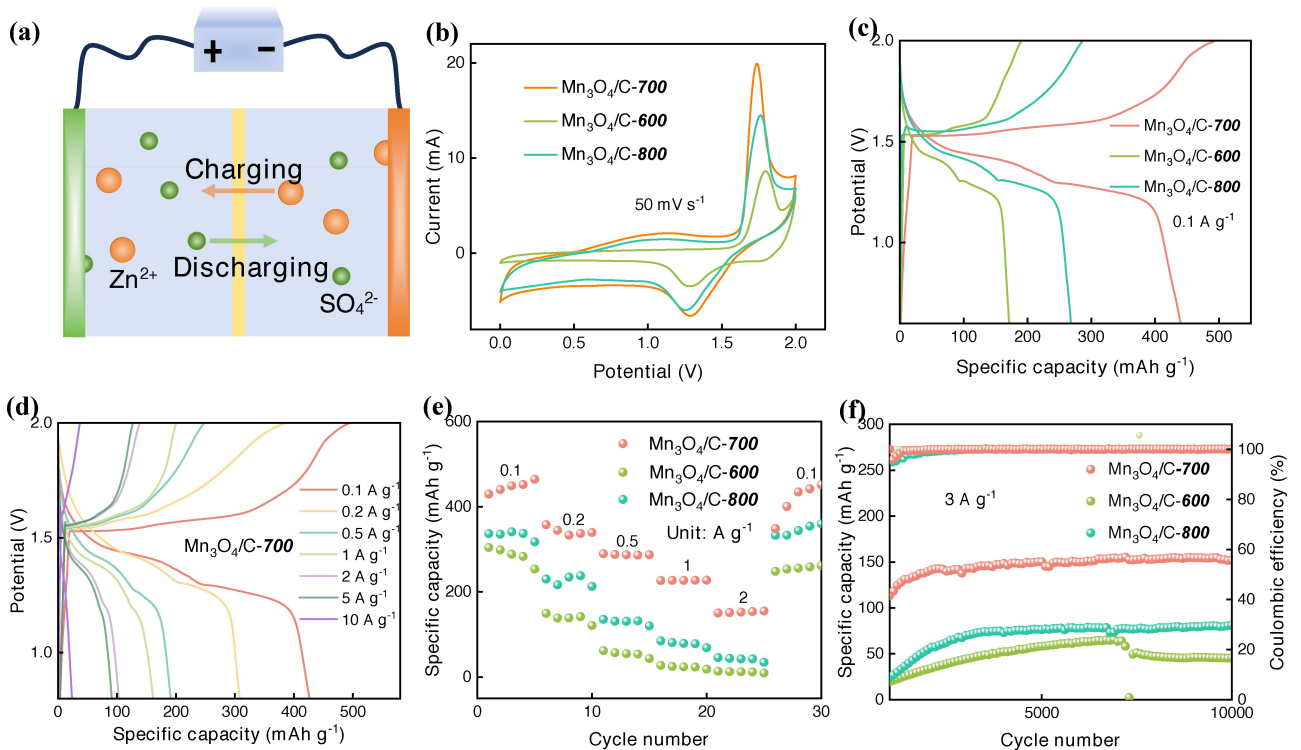


Figure 3. Electrochemical performances of the samples (a) schematic illustration of reaction mechanism of device (b) CV curves (c) and (d) GCD curves (e) rate capacity (f) long-term cycle performance.

anions are adsorbed/desorbed on the surface of $\text{Mn}_3\text{O}_4/\text{C}$ cathode. The reversible deposition/stripping of Zn^{2+} can be realized on Zn anode. Figure 3b shows the CV curves of the three electrodes at a scan rate of 50 mV s^{-1} in the $0\text{--}2$ voltage window. All electrode materials present a pair of distinct redox peaks, which correspond to the embedding and detachment of Mn^{2+} . It indicates the pseudocapacitive nature of the sample. $\text{Mn}_3\text{O}_4/\text{C-700}$ electrode shows the largest integration area, indicating that its high charge storage capacity. The constant current charge-discharge (GCD) curves of ZHCs (Figure 3c) present the specific capacitance of the devices at the same current density. The specific capacitance of $\text{Mn}_3\text{O}_4/\text{C-700}$ can reach 426.4 mAh g^{-1} at 0.1 A g^{-1} , while the $\text{Mn}_3\text{O}_4/\text{C-600}$, $\text{Mn}_3\text{O}_4/\text{C-800}$ only possess 267.8 and 171.0 mAh g^{-1} . It might be attributed to the fact that the material carbonized at 700°C present a large specific surface area and accommodates a variety of potentials. The GCD curve of the $\text{Mn}_3\text{O}_4/\text{C-700}/\text{Zn}$ (Figure 3d) indicates that the current density maintains the initial shape when the increases from 0.1 to 10 A g^{-1} . Even at 10 A g^{-1} , the ZHC still achieves a specific capacitance of 36.1 mAh g^{-1} , demonstrating the excellent reversibility and charge/discharge properties of the material.

Rate performance is an important parameter for evaluating the capacitor's storage capacity at different current densities. The specific capacities of the mixing device are 464.5 , 357.9 , 289.7 , 227.1 and 155.3 mAh g^{-1} at 0.1 , 0.2 , 0.5 , 1.0 , and 2.0 A g^{-1} , respectively (Figure 3e). Notably, a capacity of 451.9 mAh g^{-1} with a recovery rate of 97.3% is obtained when the current density returns to 0.1 A g^{-1} . The results demonstrate that the

$\text{Mn}_3\text{O}_4/\text{C-700}$ -based capacitor presents a high reversible rate capability. In addition, the $\text{Mn}_3\text{O}_4/\text{C-800}$ material possesses a specific capacity of 42.8 mAh g^{-1} at 2 A g^{-1} , which exceeds that of the $\text{Mn}_3\text{O}_4/\text{C-600}$ example (12.5 mAh g^{-1}). Meanwhile, the zinc-ion hybrid capacitor also shows outstanding cycling stability (Figure 3f). After a short activation process, the $\text{Mn}_3\text{O}_4/\text{C-700}$ material reaches a capacitance of 155.3 mAh g^{-1} at 3 A g^{-1} . It maintains 151.8 mAh g^{-1} after $10,000$ cycles, and the capacity retention rate is as high as 97.7% . Table 2 summarizes the electrochemical properties of several cathode materials. The result shows that our designed $\text{Mn}_3\text{O}_4/\text{C-700}$ electrodes outperform several other results in terms of charge/discharge capacity.

To illustrate the reason for the excellent electrochemical performance of $\text{Mn}_3\text{O}_4/\text{C-700}$ electrode, we systematically study the CV curves at different sweep rates (Figure 4a). It can be clearly observed that there is no significant change in shape as the scan rate increases from 1 to 100 mV s^{-1} , demonstrating its structural stability. As the scanning speed increases, the anodic and cathodic peaks move to high and low potentials, respectively. This may be owing to the polarization of the electrode material. From the CV curves, different peak current values (i , mA) are obtained at different voltage sweep rates (Figure 4b). It is possible to distinguish whether the device shows diffusive or pseudocapacitive behavior during charging and discharging. For electrode materials, the value of b can be calculated to determine its behavior using the equations (1):

$$i = a v^b \quad (1)$$

Table 2. The electrochemical performance of the recently reported cathode materials.

Materials	Potential/ V	Capacity/ [mAh·g ⁻¹]	Current density/ [A·g ⁻¹]	Capacity retention, cycles	Refs.
Hollow carbon spheres	0.15–1.95	87	0.5	98.0 %, 15,000	[25]
CNPK	0.2–1.8	103	0.1	100.0 %, 10,000	[33]
RuO ₂ ·H ₂ O	0.4–1.6	122	0.1	87.5 %, 10000	[34]
VO _{0.9} /C	0.2–1.8	146	1.0	84.0 %, 10,000	[35]
3DPC	0.2–1.8	194	0.5	88 %, 15000	[36]
Mn ₃ O ₄ /C-700	0–2.0	220	1.0	97.7 %, 10000	This work

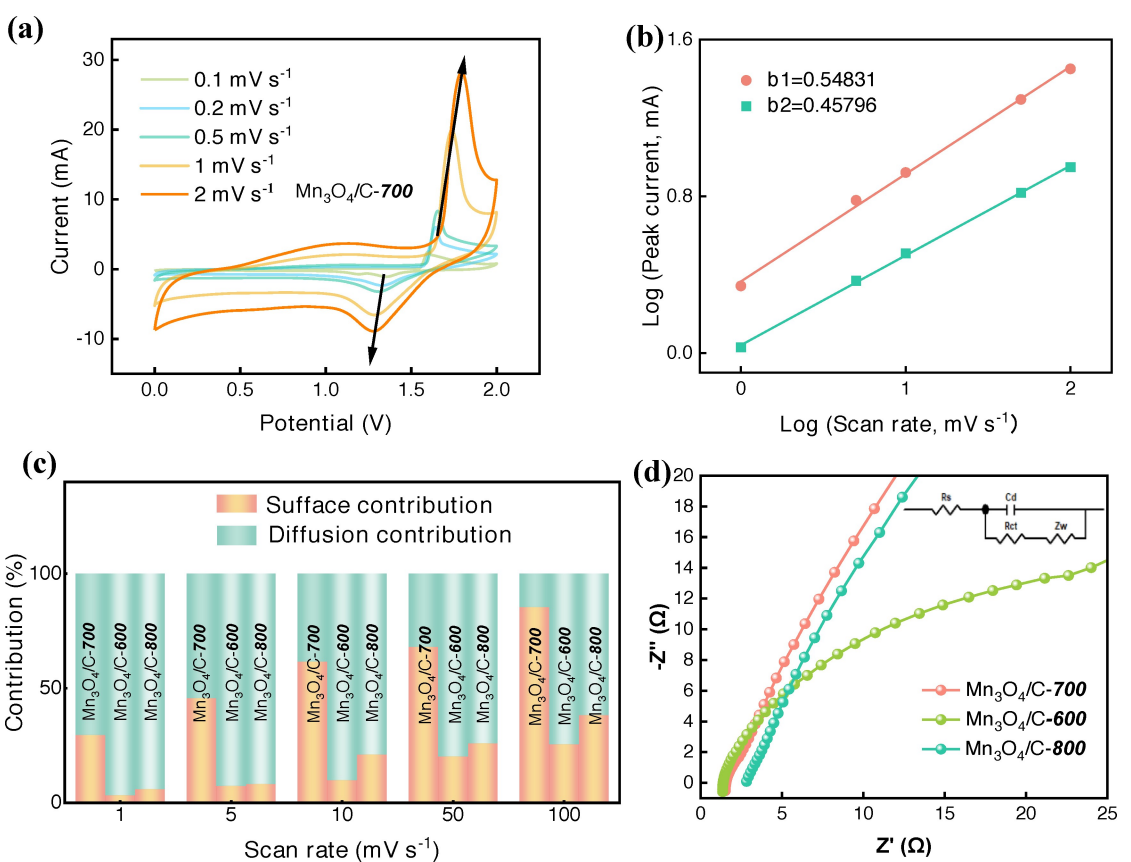


Figure 4. Electrochemical reaction kinetics of Mn₃O₄/C//Zn (a) CV (b) fitting plots of log [i] and log [v] (c) capacitive contribution ratio at various scan rates (d) EIS spectra.

If the value of $b = 0.5$, the electrode material shows battery properties; if the value of $0.5 < b < 1$, the electrode material presents both cell and pseudocapacitance properties. When $b \geq 1$, the electrode material possesses pseudocapacitive properties. The b values of the reduction and oxidation peaks of Mn₃O₄/C-700 are calculated by linear fitting. As shown in Figure 4b, the calculated b values are 0.548 and 0.458, respectively. It indicates that the charge storage mechanism is mainly determined by the ultrafast kinetic capacitance contribution. The pseudocapacitance contribution at a specific scan rate is further calculated and the procedure can be described by the following formula:^[37]

$$i(V) = k_1 v + k_2 v^{1/2} \quad (2)$$

where V is potential, and $k_1 v$ and $k_2 v^{1/2}$ represent the surface and diffusion-controlled current, respectively. The capacitance contribution of Mn₃O₄/C-700 electrode increases from 29.6 % to 85.5 % as the sweep rate increases from 1 to 100 mV s⁻¹ (Figure 4c). Moreover, the introduction of Mn ion accelerates the electrochemical kinetics of the electrodes.^[38]

EIS is also used to explore the charge transfer kinetics of Mn₃O₄/C materials. Figure 4d is the Nyquist plots of the three samples, which show large linear slopes in the low frequency region, indicating the low impedance and high ionic transfer. The semicircle in the high-frequency region represents the charge transfer resistance (R_{ct}). In specific, the Mn₃O₄/C-700

electrode shows the smallest semicircle diameter, implying a small charge transfer resistance. Carbon as an electron conductor accelerates the movement of electrons in the electrolyte and reduces the charge transfer impedance of the material.

Finally, to explore whether zinc ion capacitors present excellent performance at low temperature. We study the electrochemical performance of the assembled devices at 0 °C. From Figure 5a, the specific capacities of the Mn₃O₄/C-700 based ZHC at 0.1, 0.2, 0.5, 1, 2, 5 and 10 A g⁻¹ are 192.9, 158.3, 125.6, 109.8, 93.9, 66.7 and 47.2 mAh g⁻¹. When the current density is restored to 0.1 A g⁻¹, the discharge specific capacity can be restored to 214.4 mAh g⁻¹. It can be observed from Figure 5b that the corresponding charging/discharging curves are not distorted at different current densities, showing a superior discharge capacity. Figure 5c demonstrates a decrease in charge/discharge time compared to room temperature. This might be attributed to the decrease in solubility of the electrolyte at 0 degree. However, it shows symmetric and distinct potential plateau at different current densities (Figure 5d). This indicates excellent reversibility of the charge/discharge behavior. Figure 5e shows the cycling performance of the device at a current density of 1 A g⁻¹, respectively. It is found that the initial specific capacitance of Mn₃O₄/C-700 at 0 °C is 58.94 mAh g⁻¹ and the capacity is up to 76.73 mAh g⁻¹ after 1300 cycles.

The energy density and power density of device can be obtained by the following equations:^[39]

$$E = QU / 2m \quad (3)$$

$$P = iU / 2m \quad (4)$$

where E (Wh kg⁻¹) is the energy density and P is the power density (kW kg⁻¹). Q (Ah), U (V), i (A) and m (kg) denote the discharge capacity, operating potential, discharge current and mass loading, respectively. As can be seen in Figure 5f, the assembled capacitor presents an energy density of 464.5 Wh kg⁻¹ at a power density of 100 W kg⁻¹ (0.1 A g⁻¹). Even at 3.0 A g⁻¹, the energy density of 155.3 Wh kg⁻¹ can be maintained at 3 kW kg⁻¹. In addition, the ZHC achieves an energy density of 93 Wh kg⁻¹ at a power density of 10 kW kg⁻¹ at 0 °. The excellent electrochemical properties of device may be caused by the following reasons. First, the electrode materials with porous structure effectively shortens the ion diffusion path and accelerate the ion/electron transfer. Second, abundant mesopores provide large surface area and increase the density of active sites for redox reactions. Finally, the introduction of Mn facilitates the Faraday process to improve the electrochemical kinetics. Therefore, the Mn₃O₄/C-700//Zn devices present highly synergistic energy storage properties.

3. Conclusions

In summary, we have synthesized the Mn₃O₄/C-700 by using Mn-BDC precursor at a high-temperature pyrolysis under argon atmosphere. Their high specific surface area and abundant pore structure provide more active sites for electrochemical reactions. At the same time, it facilitates the pseudocapacitive

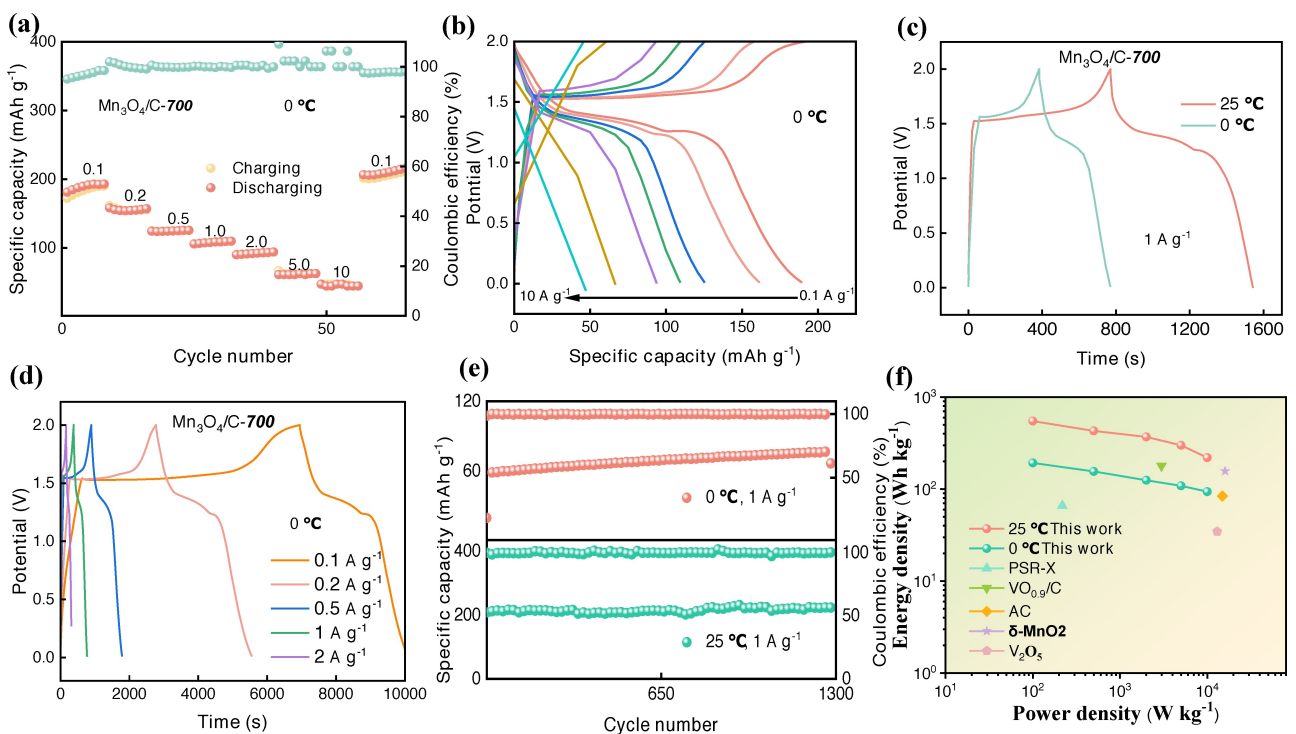


Figure 5. Low-temperature electrochemical performance of ZHCs (a) rate capacity (b) specific capacity at various current (c) and (d) charging/discharging curve (e) cycle performance (f) Ragone plot of several electrode materials for ZHCs.

reaction between the electrode material and the electrolyte ions. The presence of carbon material enhances the electrical conductivity of the electrode, which accelerates the transfer rate of ions and electrons during the electrochemical reaction. The $\text{Mn}_3\text{O}_4/\text{C}$ -700-based ZHCs show high energy and power densities, as well as an extraordinarily long cycling life and high-capacity retention rate. Moreover, the material maintains outstanding rate and charge/discharge performance at 0 °C.

Acknowledgements

This project is supported by Natural Science Foundation of China (No. 52172218) and the Open Research Subject of Hebei Key Laboratory of Dielectric and Electrolyte Functional Material, Northeastern University at Qinhuangdao (No. HKDEFM2023204).

Conflict of Interests

The authors declare no conflict of interests.

Data Availability Statement

The data that support the findings of this study are available from the corresponding author upon reasonable request.

Keywords: Zinc ion hybrid capacitor • Metal-organic frameworks • Mn_3O_4 electrode • Energy density • Specific capacity

- [1] L. B. Dong, W. Yang, W. Yang, Y. Li, W. J. Wu, G. X. Wang, *J. Mater. Chem. A*, **2019**, *7*, 13810–13832.
- [2] L. Miao, Y. K. Lv, D. Z. Zhu, L. C. Li, L. H. Gan, M. X. Liu, *Chin. Chem. Lett.* **2023**, *34*, 107784.
- [3] L. Wang, M. K. Peng, J. R. Chen, X. N. Tang, L. B. Li, T. Hu, K. Yuan, Y. W. Chen, *ACS Nano*, **2022**, *16*, 2877–2888.
- [4] F. Wei, Y. C. Wei, J. F. Wang, M. C. Han, Y. H. Lv, *Chem. Eng. J.* **2022**, *450*, 137919.
- [5] B. Sun, P. Xiong, U. Maitra, D. Langsdorf, K. Yan, C. Y. Wang, J. Janek, D. Schröder, G. X. Wang, *Adv. Mater.* **2020**, *32*, 1903891.
- [6] J. H. Cao, Y. Z. Hu, Y. Y. Zhu, H. J. Cao, M. Q. Fan, C. H. Huang, K. Y. Shu, M. X. He, H. C. Chen, *Chem. Eng. J.* **2021**, *405*, 126928.
- [7] J. L. Jin, X. S. Geng, Q. Chen, T. L. Ren, *Nano-Micro Lett.* **2022**, *14*, 64.
- [8] J. Yin, W. L. Zhang, N. A. Alhebshi, N. Salah, H. N. Alshareef, *Adv. Energy Mater.* **2021**, *11*, 2100201.
- [9] X. Y. Liu, M. D. Wang, A. Umarb, X. Wu, *Dalton Trans.* **2023**, *52*, 10457–10464.
- [10] J. J. Zhang, X. Wu, *Int. J. Miner. Metall. Mater.* **2024**, *31*, 179–185.

- [11] H. C. He, J. C. Lian, C. M. Chen, Q. T. Xiong, C. C. Li, M. Zhang, *Nano-Micro Lett.* **2022**, *14*, 106.
- [12] X. W. Wang, Y. C. Sun, W. C. Zhang, X. Wu, *Chin. Chem. Lett.* **2023**, *34*, 107593.
- [13] Y. J. Ren, S. W. Zhang, B. S. Yin, J. R. Loh, Y. X. Ding, X. J. Huang, J. Z. Li, H. Li, T. Y. Ma, *Batteries & Supercaps* **2023**, *6*, 2300132.
- [14] D. Chen, H. L. Chen, C. F. Du, L. Liu, H. B. Geng, H. Yu, X. H. Rui, *J. Mater. Chem. A*, **2022**, *10*, 5479–5487.
- [15] G. Q. Sun, H. S. Yang, G. F. Zhang, J. Gao, X. T. Jin, Y. Zhao, L. Jiang, L. T. Qu, *Energy Environ. Sci.* **2018**, *11*, 3367–3374.
- [16] H. Wang, M. Wang, Y. B. Tang, *Energy Storage Mater.* **2018**, *13*, 1–7.
- [17] Y. Li, X. Y. Peng, X. Li, H. Duan, S. Y. Xie, L. B. Dong, F. Y. Kang, *Adv. Mater.* **2023**, *35*, 2300019.
- [18] H. Tang, J. J. Yao, Y. R. Zhu, *Adv. Energy Mater.* **2021**, *11*, 2003994.
- [19] D. Sui, M. N. Wu, K. Y. Shi, C. L. Li, J. W. Lang, Y. L. Yang, X. Y. Zhang, X. B. Yan, Y. S. Chen, *Carbon*, **2021**, *185*, 126.
- [20] R. W. Cui, Z. W. Zhang, H. J. Zhang, Z. H. Tang, Y. H. Xue, G. Z. Yang, *Nanomaterials*, **2022**, *12*, 386.
- [21] X. Liu, Y. J. Sun, Y. Tong, X. Y. Wang, J. F. Zheng, Y. A. Wu, H. Y. Li, N. Y. Hou, *Nano Energy*, **2021**, *86*, 106070.
- [22] P. G. Liu, Y. Gao, Y. Y. Tan, W. F. Liu, Y. P. Huang, J. Yan, K. Y. Liu, *Nano Res.* **2019**, *12*, 2835.
- [23] J. J. Zhong, L. Qin, J. L. Li, Z. Yang, K. Yang, M. J. Zhang, *Int. J. Miner. Metall. Mater.* **2022**, *29*, 1061.
- [24] L. Dong, X. Ma, Y. Li, L. Zhao, W. Liu, J. Cheng, C. Xu, B. Li, Q. H. Yang, F. Kang, *Energy Storage Mater.* **2018**, *13*, 96.
- [25] S. Chen, L. Ma, K. Zhang, M. Kamruzzaman, C. Zhi, J. A. Zapien, *J. Mater. Chem. A*, **2019**, *7*, 7784.
- [26] L. Q. Huang, Y. Xiang, M. W. Luo, Q. Zhang, H. Zhu, K. Y. Shi, S. P. Zhu, *Carbon*, **2021**, *185*, 1–8.
- [27] J. X. Li, Y. S. Gao, R. Holze, S. Y. Li, E. Mijowska, X. C. Chen, *Batteries & Supercaps* **2023**, *6*, 2300175.
- [28] Y. Z. Zhang, Tao Cheng, Y. Wang, W. Y. Lai, H. Pang, W. Huang, *Adv. Mater.* **2016**, *28*, 5241.
- [29] L. Tong, C. Wu, J. Hou, Z. Zhang, J. Yan, G. Wang, Z. Li, H. Che, Z. Xing, X. Zhang, *J. Electroanal. Chem.* **2023**, *928*, 117074.
- [30] S. L. Wang, Q. Wang, W. Zeng, M. Wang, L. M. Ruan, Y. N. Ma, *Nano-Micro Lett.* **2019**, *11*, 70.
- [31] M. Zhao, S. L. Li, X. Wu, S. H. Luo, *Adv. Mater. Technol.* **2024**, *9*, 2400125.
- [32] C. J. Chen, Z. W. Li, Y. H. H. J. Liao, L. Y. Wu, H. Dou, X. G. Zhang, *Batteries & Supercaps* **2021**, *4*, 680–686.
- [33] H. Zhang, Z. Chen, Y. Zhang, Z. Ma, Y. Zhang, L. Bai, L. Sun, *J. Mater. Chem. A*, **2021**, *9*, 16565.
- [34] L. B. Dong, W. Yang, W. Yang, C. Y. Wang, Y. Li, C. J. Xu, S. W. Wan, F. R. He, F. Y. Kang, G. X. Wang, *Nano-Micro Lett.* **2019**, *11*, 94.
- [35] Y. Liu, A. Umar, X. Wu, *Rare Met.* **2022**, *41*, 2985–2991.
- [36] Y. S. Wang, J. Yang, S. Y. Liu, X. G. Che, S. J. He, Z. B. Liu, M. Wang, X. T. Wang, J. S. Qiu, *Carbon*, **2023**, *201*, 624–632.
- [37] X. Y. Liu, M. D. Wang, X. Wu, *Molecules*, **2022**, *27*, 7344.
- [38] D. D. Zhang, J. Cao, X. Y. Zhang, N. Insin, S. M. Wang, J. T. Han, Y. S. Zhao, J. Q. Qin, Y. H. Huang, *Adv. Funct. Mater.* **2021**, *31*, 2009412.
- [39] Y. Liu, X. Wu, *J. Energy Chem.* **2023**, *87*, 334–341.
- [40] D. Chen, H. L. Chen, C. F. Du, L. Liu, H. B. Geng, H. Yu, X. H. Rui, *J. Mater. Chem. A*, **2022**, *10*, 5479–5487.

Manuscript received: March 26, 2024

Revised manuscript received: May 6, 2024

Accepted manuscript online: May 7, 2024

Version of record online: June 14, 2024